

1 **Water masses distribution offshore the Sabrina Coast (East Antarctica)**

2 Bensi Manuel¹, Kovačević Vedrana¹, Donda Federica¹, O'Brien Philip Edward², Armbrecht Linda³, Armand Kay Leanne⁴

3

4 ¹ National Institute of Oceanography and Applied Geophysics (OGS), Trieste, 34010, Italy;

5 ² Department of Environmental Sciences, Macquarie University, Sydney, Australia;

6 ³ Institute for Marine and Antarctic Studies, University of Tasmania, Battery Point TAS 7004, Australia;

7 ⁴ Australian National University, Canberra, Australia;

8 *Correspondence to:* M. Bensi (mbensi@inogs.it)

9 **Abstract**

10 Current glacier melt rates in West Antarctica substantially exceed those around the East Antarctic margin. The exception is Wilkes
11 Land where, e.g., Totten Glacier, underwent significant retreat between 2000 and 2012, underlining its sensitivity to climate
12 change. This process is strongly influenced by ocean dynamics, which in turn changes in accordance with the evolution of the ice
13 caps. Here, we present new oceanographic data (temperature, salinity, and dissolved oxygen) collected during austral summer
14 2017 offshore the Sabrina Coast (East Antarctica) from the continental shelf break to ca 3000 m depth. This area is characterized
15 by very few oceanographic in situ observations.

16 The main water masses of the study area, identified by analysing thermohaline properties, are: the Antarctic Surface Water with
17 potential temperature $\theta > -1.5$ °C and salinity $S < 34.2$ ($\sigma_0 < 27.55$ kg m⁻³), the Winter Water with $-1.92 < \theta < -1.75$ °C and $34.0 < S < 34.5$ (potential density, $27.55 < \sigma_0 < 27.7$ kg m⁻³), the modified Circumpolar Deep Water with $\theta > 0$ °C and $S > 34.5$ ($\sigma_0 > 27.7$ kg m⁻³), and Antarctic Bottom Water with $-0.50 < \theta < 0$ °C and $34.63 < S < 34.67$ ($27.83 < \sigma_0 < 27.85$; neutral density $\gamma^n > 28.30$ kg m⁻³). The latter is a mixture of dense waters from the Ross Sea and Adélie Land continental shelves. Such waters are
21 influenced by the mixing processes they undergo as they move westward along the Antarctic margin, also interacting with the
22 warmer Circumpolar Deep Water.

23 The spatial distribution of water masses offshore the Sabrina Coast also appears to be strongly linked with the complex morpho-
24 bathymetry of the slope and rise area, supporting the hypothesis that downslope processes contribute to shaping the architecture
25 of the distal portion of the continental margin.

26

27 **Short summary (plain text)**

28 The Totten Glacier (Sabrina Coast, East Antarctica) has undergone significant retreat in recent years, underlining its sensitivity to
29 climate change and its potential contribution to global sea-level rise. The melting process is strongly influenced by ocean dynamics,

30 while the spatial distribution of water masses in this region appears to be linked to the complex morpho-bathymetry, which also
31 supports the hypothesis that downslope gravity currents contribute to shaping the architecture of the continental margin.

32 **1 Introduction**

33 [1] Polar regions are key components of Earth's climate system and are particularly sensitive to ongoing climate change effects
34 induced by anthropogenic pressures. It has been estimated that the full melting of all Antarctic ice has a sea level equivalent (SLE)
35 of ~58 m (Fretwell et al., 2013).

36 Understanding Earth's climate processes as well as their future projections depends on the constant collection and interpretation
37 of long-term scientific data and palaeoclimatic records. Therefore, studying long-term records from polar regions is key (e.g.,
38 Masson-Delmotte et al., 2013) to have a more complete understanding of the region's past climate variability (e.g., Escutia et al.,
39 2019). Within this frame, quantifying sea-level rise associated with global warming is crucial, and the accuracy of such
40 quantifications ultimately depends on our knowledge of the response of polar regions to global warming. In fact, there is still
41 significant uncertainty in estimates around sea-level rise, as Church et al. (2013) reported in the IPCC AR5 Sea Level Chapter.
42 They delineate that significant challenges remain in understanding and predicting processes related to the dynamic response of
43 Antarctic marine-terminal glaciers and marine sectors. The Antarctic ice sheet response to current climate forcing can be elucidated
44 by examining how the ice sheet had behaved in response to similar climate forcings in the past. In spite of the significant effort in
45 putting the estimates together, the IPCC report expresses only medium confidence in estimating the contribution of Antarctic ice
46 melt to sea levels during the last major warm episode, e.g. the Last Interglacial period, ca 129k to 116k years ago (Masson-
47 Delmotte et al., 2013).

48 Marine processes change in accordance with the evolution of the ice caps and vice versa, especially in those areas where glaciers
49 are grounded below sea level. This condition occurs not only in West Antarctica, but also in several portions of East Antarctica
50 (e.g., Adelie Land, Rignot et al., 2011), including the Sabrina Coast. Here, the Totten Glacier, the downstream end of the vast
51 Aurora subglacial basin, is largely grounded below sea level and hence susceptible to rapid ocean-driven ice sheet basal melting
52 (Pritchard et al., 2009; Roberts et al., 2011; Young et al., 2011; Rignot et al., 2013; Aitken et al., 2016; Hirano et al., 2021). Totten
53 Glacier is, indeed, exposed to temperatures up to 3 °C above the ice shelves' melting point (Rintoul et al., 2016). The Aurora
54 subglacial basin today also hosts an active subglacial hydrological system that drains basal meltwater to the ocean (Wright et al.,
55 2012).

56 [2] According to Silvano et al. (2018), while relatively warm waters (> 0°C) flood the continental shelves in West Antarctica
57 driving rapid basal melt of ice shelves, the ice shelves in East Antarctica experience relatively low rates of basal melt because they
58 are influenced by cooler waters (< 0°C). However, the Totten Glacier is an exception, since the melting rates of this glacier and of
59 the nearby Moscow University ice shelf (MUIS) are among the fastest in the East Antarctic Ice Sheets (Khazendar et al., 2013; Li
60 et al., 2015; Mohajerani et al., 2018): the glacier draining into MUIS shows a 3 Gt/y loss in 1979–2003 and a 0.3 Gt/y gain in

61 2017, whereas Totten Glacier loss has increased through time from 5.7 Gt/y in 1979–2003 to 7.3 Gt/y in 2003–2017 (Rignot et al.,
62 2019). These changes are enhanced by incursions of relatively warm modified Circumpolar Deep Water (mCDW) to the
63 continental shelf and to the glacier grounding line, favoured by wind stress, local eddies, and bathymetric constraints (Rintoul et
64 al., 2016; Silvano et al., 2016; 2017; Nitsche et al., 2017; Greene et al., 2017; Hirano et al., 2021). In fact, a deep and extensive
65 pool of water with maximum temperature of $\sim 0.7^{\circ}\text{C}$ has been identified at the outer continental shelf over a wide bathymetric
66 depression at depths below 400–500 m (Nitsche et al., 2017). Ice loss can locally be also favoured by low levels of sea ice and
67 Dense Shelf Water production in the Antarctic polynyas (Tamura et al., 2008), although there is still no clear evidence, surprisingly,
68 of dense shelf water production in the Dalton polynya, east of the Totten ice shelf (Silvano et al., 2018). Rignot et al. (2019)
69 reported that Totten Glacier holds an ice volume that translates into a SLE of 3.85 m. The mCDW, being the major heat source on
70 the Sabrina Coast continental shelf, is characterized by a temperature larger than -0.4°C and a salinity around 34.5–34.6 (Silvano
71 et al., 2017), and comprises the bottom layer of the water column. This appears to be different from other coastal areas of East
72 Antarctica, where the bottom layer is usually occupied by colder and denser Shelf Water (Bindoff et al., 2000; Greenbaum et al.,
73 2015). Studies of rapidly retreating outlet glaciers in the Amundsen Sea have shown a major role of the mCDW in transporting
74 heat from the deep ocean onto the shelf, leading to enhanced glacier melting (Smith et al., 2011; Pritchard et al., 2012). This
75 process has also been suggested as a possible cause for the rapid melting of Totten Glacier (e.g., Williams et al., 2011; Pritchard
76 et al., 2012; Greene et al., 2017), but other mechanisms have been also suggested. Pritchard et al. (2012) invoked that changes in
77 the circum-Antarctic wind field and its effects on upwelling around the continent cause the rapid basal melting of the Totten
78 Glacier. Also, Khazendar et al. (2013) and Gwyther et al. (2014) have argued that this enhanced melting is the result of complex
79 interactions between oceanic and shelf water masses at the base of the ice. In particular, Gwyther et al. (2014) suggested that the
80 ice melting varies on seasonal and interannual timescales, with increased ice melt of the Totten Glacier coinciding with a reduced
81 strength of the nearby Dalton polynya. These studies rely heavily on satellite observations and bathymetry of the regions, e.g., the
82 1 km horizontal grid resolution obtained through the General Bathymetric Chart of the Oceans (GEBCO) used for oceanographic
83 models (Gwyther et al., 2014). The GEBCO grid has 2 ship tracks in the critical 150 km by 200 km area seaward of the Totten
84 Glacier, meaning that most of the grid is a "best guess".

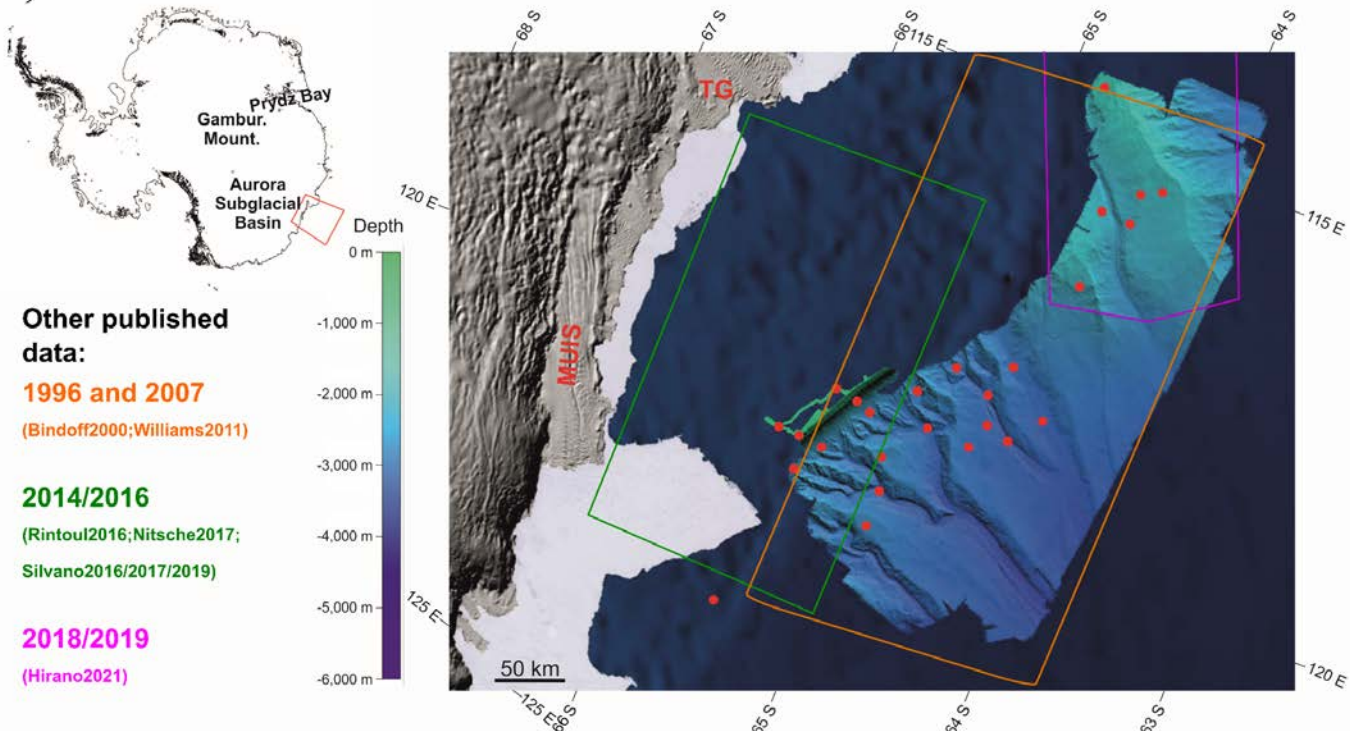
85 [3] The Antarctic ice sheet nucleated in the higher elevations of the Gamburtsev Mountains and first reached the ocean near the
86 Sabrina Coast and Prydz Bay (Huybrechts 1993; DeConto & Pollard 2003). Marine-terminating glaciers existed at the Sabrina
87 Coast by the early-middle Eocene (ca. 56–41 Ma), implying the occurrence of ice caps before the emplacement of continental-
88 scale ice sheets (Gulick et al., 2017). The first preserved evidence of grounded ice on the Sabrina Coast shelf is suggested to be
89 Late Eocene in age (ca. 38 Ma; Gulick et al., 2017). The climate evolution of the Wilkes Land margin, and thus of the Sabrina
90 Coast, from the pre-glacial Era to the present time comprises three main key periods: i) pre-glacial conditions (Phase 1 reported in
91 Donda et al., 2007); ii) growth and development of a polythermal, highly dynamic ice sheet (Phases 2 and 3 in Donda et al., 2007),
92 and iii) transition to polar conditions (Phase 4 in Donda et al., 2007). This overall picture is well supported by several Antarctic
93 and sub-Antarctic stratigraphic records, e.g., the Deep Sea Drilling Program Leg 28, Cape Roberts Drilling Project, Ocean Drilling

94 Program Legs 119, 188, and 189 and International Ocean Discovery Program Leg 318 (Donda et al., 2020). Compared to other
95 areas, the Sabrina Coast seismostratigraphy suggests that downslope processes contributed to shaping the distal margin architecture
96 even during its latest development stages (i.e., Phase 4), when glacial meltwater-related fluxes were able to erode and deliver
97 sediments to the rise area (Donda et al., 2020). The continental slope and rise of the Sabrina Coast reveal remarkable differences
98 between the eastern and western areas, as also highlighted by the present-day bathymetry (Fig. 1). The western sector is shallower
99 and characterized by the presence of two prominent NE-SW trending ridges, separated by a low sinuosity narrow submarine
100 canyon flanked with terraces. Here, one of these bathymetric highs favours the generation of a cyclonic gyre centered on 115°E,
101 just north of the shelf break (Wakatsuchi et al., 1994). Armand et al. (2018) described the eastern facing slopes of the ridges (Fig.
102 1) as smooth seafloor with significant evidence of mass movement (e.g., slump scars and debris runout fields), while their western
103 facing slopes are gullied terrain (with a gully depth range of up to 15 m). In fact, the associated canyon is not receiving a high
104 proportion of downslope turbidity currents, rather being fed by slumping on the adjacent ridge flanks (O'Brien et al., 2020). The
105 eastern ridge was reported as having a lower slope than the western ridge, and being dominated by slump scars.
106 The eastern sector, instead, is characterized by a complex network of erosional channels and it is shaped by dendritic canyons,
107 which meander and bend sharply to then join less sinuous main channels, the floors of which contain terraces and closed
108 depressions (O'Brien et al., 2020). The ridges between canyons are clearly tied to their adjoining canyons and formed by westward
109 advection of fine sediment lofted from turbidity currents and deposition of pelagic sediment (O'Brien et al., 2020). The western
110 and the eastern areas are separated by a broad depression linked with one of the dendritic canyons near the lower slope. The upper
111 slope consists of a smooth to gullied apron, downslope of which the canyon heads begin. The shelf break occurs at depths of 480
112 - 510 m.
113 [4] This paper aims at describing the thermohaline structures from the continental shelf break to about 3000 m depth identified in
114 the offshore area along the Sabrina Coast, by analysing physical oceanographic data collected in 2017 during a multidisciplinary
115 Antarctic expedition (see below).

116 **2 The oceanographic dataset: instrumentation and data processing**

117 Oceanographic data presented in this paper were collected offshore the Sabrina coast, between 113°E and 122°E and 66°S and
 118 64°S (Fig. 1) during the marine geoscience expedition “Interactions of the Totten Glacier with the Southern Ocean through multiple
 119 glacial cycles” (IN2017_V01) (see Armand et al., 2018). This expedition took place between 14 January and 7 March 2017 on
 120 board the Australian Marine National Facility (MNF) Research Vessel *Investigator*.

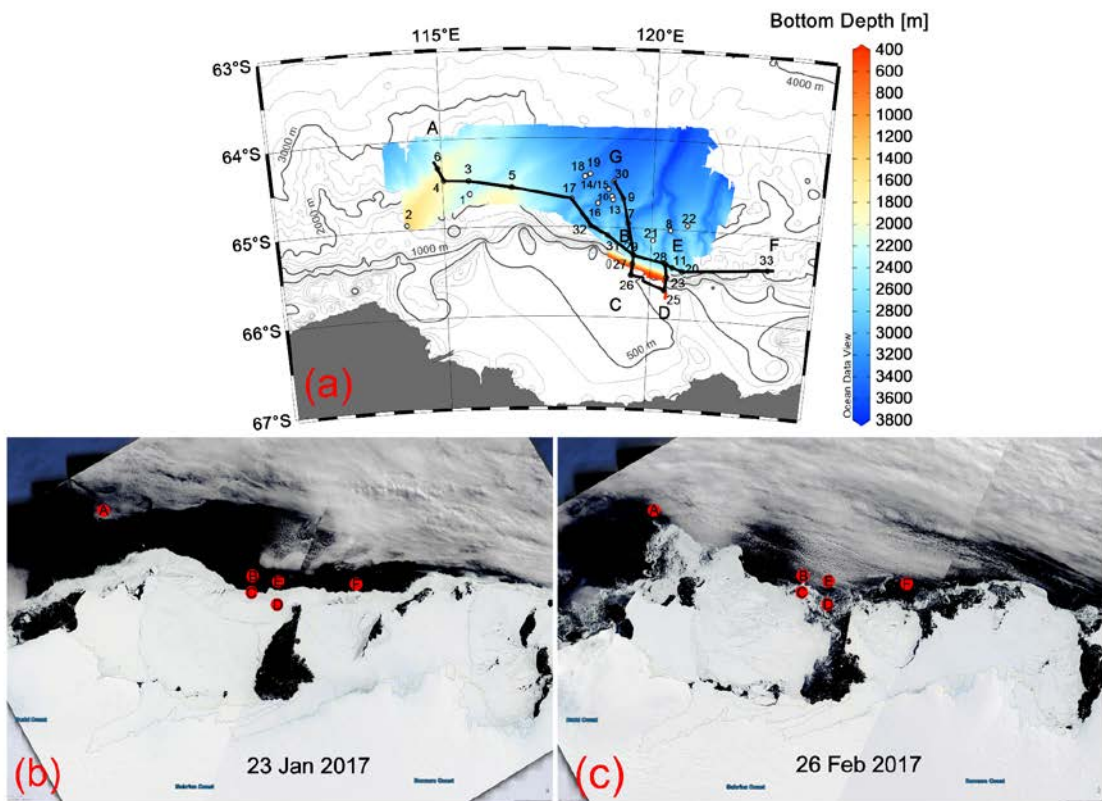
121



122
 123 **Figure 1** - Sabrina Seafloor Survey area. Red dots indicate CTD casts collected during the IN2017_V01 cruise. Coloured
 124 polygons, instead, indicate areas where other already published hydrological data have been taken (reference years and related
 125 articles are indicated on the left). The high resolution bathymetry obtained from multibeam data acquired during the IN2017_V01
 126 cruise (from O'Brien et al., 2020) is superimposed over the lower resolution bathymetry from the International Bathymetric Chart
 127 of the Southern Ocean. On land, the terrain map comes from the Reference Elevation Model of Antarctica (REMA, Howat et al.,
 128 2019). The colorbar on the left refers to the high resolution multibeam bathymetry.

129
 130 We take into account 31 Conductivity-Temperature-Depth (CTD) vertical profiles (labeled 1-11, 13-23, 25-33) acquired in the
 131 study region (Fig. 2) using a Seabird SBE 9plus (pump-controlled) CTD and SBE 11plus V2 Deck Unit. The CTD was integrated
 132 with a SBE32 Carousel Water Sampler equipped with 36 Niskin bottles (OceanTest Equipment Inc. Florida; 12-L capacity each
 133 one, mounted on the rosette sampler), with additional sensor for measuring dissolved oxygen concentration (DO, SBE43), and

134 altimeter (PA500). The Commonwealth Scientific and Industrial Research Organisation (CSIRO) supplied calibration factors that
135 were used to compute pressure, temperature, and conductivity/salinity values. Data were subjected to automated quality control
136 (QC) to remove spikes and out-of-range values (see https://www.marine.csiro.au/data/reporting/get_file.cfm?eov_pub_id=1512,
137 last access on October 26, 2021), while maintaining true data features. An additional filter was applied to the data to evaluate the
138 median and standard deviation of the conductivity over a moving window. This has made it possible to detect extreme changes in
139 the sensor values characteristic of the noise induced by spikes. The conductivity calibration was based on two deployment
140 groupings, due to sensor changes during the voyage, and it was based upon the comparison between conductivity data obtained
141 from CTD and water samples (104 of the total of 151 water samples taken during deployments). The final calibration for casts 1-
142 13 from the secondary sensor had a standard deviation (std) of 0.001 psu, while the final calibration for casts 14-33 from the
143 secondary sensor had a std of 0.002 psu. Water samples were also collected and used to compute new estimates of DO calibration
144 coefficients, obtained by applying a linear regression. A single calibration group from each sensor was used with the associated
145 SBE43 up-cast data. The DO calibration had a std of 0.85911 μM with a good agreement between the sensor and bottle data. Based
146 on the results obtained from the calibration procedure, the final dataset was obtained after 1 dbar binned averaged data from the
147 secondary sensors (primary sensor for DO). Note that seven CTD profiles (casts 1, 2, 11, 13, 14, 15, and 18, see Fig. 2a) stopped
148 before reaching the seafloor (between 200 and 700 m, e.g., for testing the new sensor settings). Potential temperature (θ , $^{\circ}\text{C}$) and
149 potential density anomaly (σ_0 , kg m^{-3} , referred to 0 dbar), and neutral density (γ^n , kg m^{-3}) were calculated using the toolbox TEOS-
150 (<http://www.teos-10.org/software.htm>). We use σ_0 when considering the property distribution in the upper 500 m, and where
151 the specific σ_0 values determine and delimit specific water masses within the upper layers. However, the depth range of our study
152 area is wide, and σ_0 errors augment with depth, therefore γ^n for the entire vertical range along vertical sections is used instead to
153 depict the property distributions. Neutral density (γ^n) is a function of temperature, salinity, pressure, latitude and longitude, where
154 the reference level is slightly adjusted at each point to compensate for the nonlinearity of the equation of state, hence it can be
155 considered a locally-referenced potential density. Some figures were created using Ocean Data View (ODV; Schlitzer, 2021).
156 More detailed information on instrumentation and quality control procedure are available at
157 https://www.marine.csiro.au/data/trawler/survey_details.cfm?survey=IN2017_V01 (last access on October 26, 2021).
158 Finally, satellite images (MODIS - Moderate-resolution Imaging Spectroradiometer, Corrected Reflectance imagery) were used
159 to highlight both the evolution of sea ice within the period covered by the IN2017_V01 cruise and the extension of the Dalton
160 Polynya (Fig. 2b,c), the open water surrounded by sea ice in the vicinity of Totten Glacier and MUIS. This is one of the largest
161 Antarctic coastal polynya, with its wintertime average area of $3.7 \pm 2.0 \ 10^3 \text{ km}^2$ ($6.5 \ 10^3 \text{ km}^2$ at the time of the cruise; Fig. 2b,c),
162 extending in the prevalent downwind direction (see e.g., Arroyo et al., 2019). Satellite images used in this work are freely available
163 from the NASA Worldview application (<https://worldview.earthdata.nasa.gov>), part of the NASA Earth Observing System Data.
164 The spatial imagery resolution is 250 m, and the temporal resolution is daily.



165
166 **Figure 2** - CTD stations map and color-coded high resolution bathymetry collected during the IN2017_V01 cruise (from O'Brien
167 *et al.*, 2020), superimposed over the International Bathymetric Chart of the Southern Ocean (contour lines). Positions A, B, C, D,
168 E, F, and G denote along-slope and cross-slope transects (a). The same positions A-F (red dots) along the ice edge are
169 superimposed on satellite images (MODIS Corrected Reflectance imagery freely available from
170 <https://worldview.earthdata.nasa.gov/>) taken on 23 January (b) and 26 February 2017 (c), which show the temporal evolution of
171 the sea ice extension in the study region at the beginning and at the end of the IN2017_V01 cruise.

172 3 Thermohaline patterns in the study region

173 3.1 Typical water masses

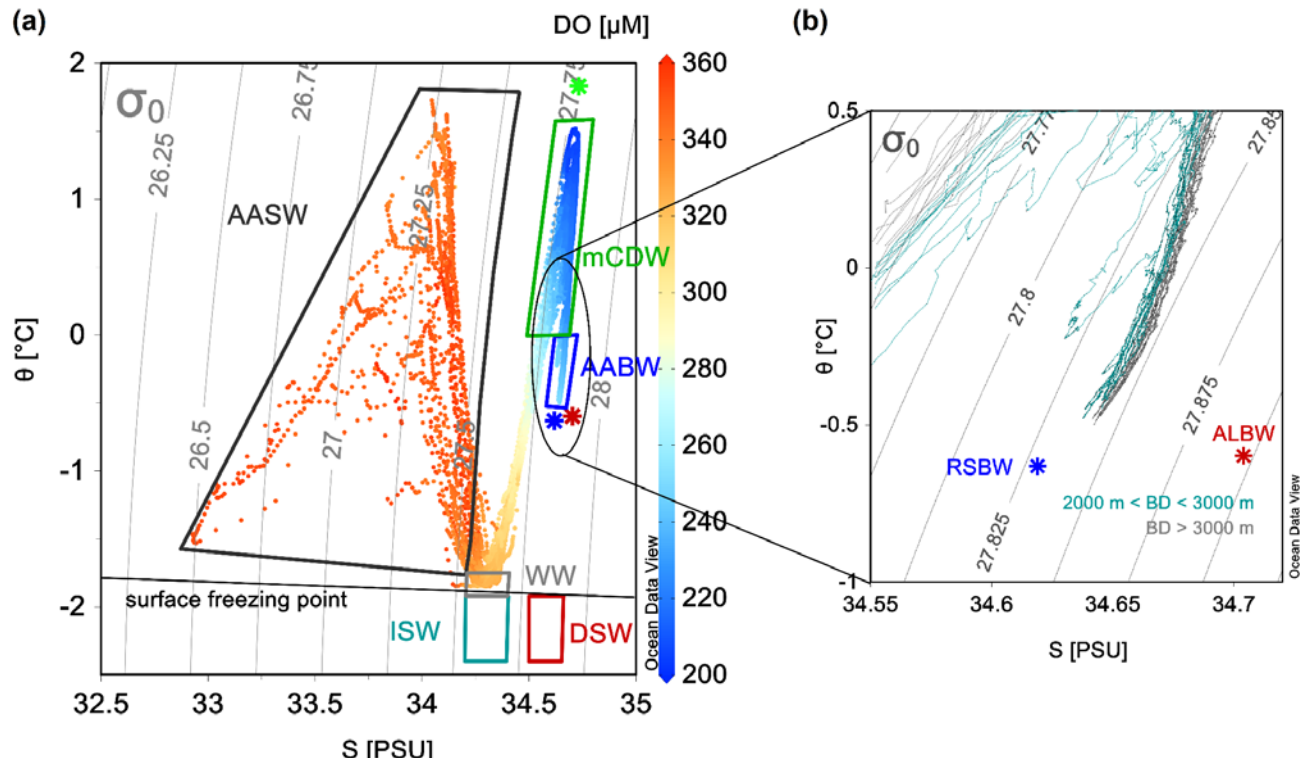
174 CTD casts are distributed over the continental slope and rise, offshore the area delimited by Totten Glacier and MUIS (Fig. 2).
175 The main water masses are identified by analysing their θ -S (and DO) properties (Fig. 3) and classified according to Silvano *et al.*
176 (2017, 2020). They are: Antarctic Surface Water (AASW) with $\theta > -1.5$ °C and $S < 34.2$ ($\sigma_\theta < 27.55$), Winter Water (WW) with -

177 $1.92 < \theta < -1.75$ and $34.0 < S < 34.5$ ($27.55 < \sigma_\theta < 27.7 \text{ kg m}^{-3}$), and mCDW, with $\theta > 0 \text{ }^\circ\text{C}$ and $S > 34.5$ ($\sigma_\theta > 27.7 \text{ kg m}^{-3}$). The
178 AASW and WW are the most ventilated and therefore have the highest dissolved oxygen values. Acquired data do not reveal the
179 presence of water with characteristics either of Ice Shelf Water (ISW, $\theta < -1.92 \text{ }^\circ\text{C}$, $S < 34.5$, $27.55 < \sigma_\theta < 27.7 \text{ kg m}^{-3}$) or Dense
180 Shelf Water (DSW, $\theta < -1.92 \text{ }^\circ\text{C}$, $S > 34.5$, $\sigma_\theta > 27.7 \text{ kg m}^{-3}$). In particular, the former is found close to the two ice shelves, and
181 the latter forms within the polynyas, because of the intense cooling and brine rejection processes that can take place there. AASW
182 comprises a wide range of both temperature and salinity. It is warm due to summer heating, and fresh due mainly to sea ice melting.
183 The WW occupies a homogeneous layer of the water column formed as a result of convection on the shelf during the previous
184 winter. The mCDW is a relatively warm and salty water mass that can access the outer continental shelf through a section of the
185 shelf break over 500 m depth (Nitsche et al., 2017), reaching the ice shelf cavity through a recently discovered oceanic entry route
186 (Greenbaum et al., 2015) and causing ice melt. The thermohaline properties associated with the densest waters are attributed to
187 the Antarctic Bottom Water (AABW, with $-0.50 < \theta < 0 \text{ }^\circ\text{C}$, $34.63 < S < 34.67$, $27.83 < \sigma_\theta < 27.85 \text{ kg m}^{-3}$, and $\gamma^n > 28.30 \text{ kg m}^{-3}$).
188 The AABW in this part of the Australian Antarctic Basin (AAB) is a mixture of the local and remote dense waters, namely the
189 Adélie Land Bottom Water (ALBW) and Ross Sea Bottom Water (RSBW, see e.g., Silvano et al., 2020), both of which have
190 distinct characteristics in their source regions (Thomas et al., 2020). The most recent typical θ - S average values encountered during
191 2018 in the AAB were $-0.599 \text{ }^\circ\text{C}/34.704$ for the RSBW, and $-0.632 \text{ }^\circ\text{C}/34.619$ for the ALBW (Thomas et al., 2020). We argue
192 that these endmember values are representative also for the conditions encountered in 2017. However, thermohaline properties
193 reported for the AABW in 2017 in our study area (Fig. 3) were slightly higher ($\sim +0.10 \text{ }^\circ\text{C}$ and $+0.05$ for θ and S , respectively)
194 than those referred to the mentioned endmembers, reflecting the mixing process that bottom waters experience as they move
195 westwards along the Antarctic margin far from their area of origin.

196

197

198

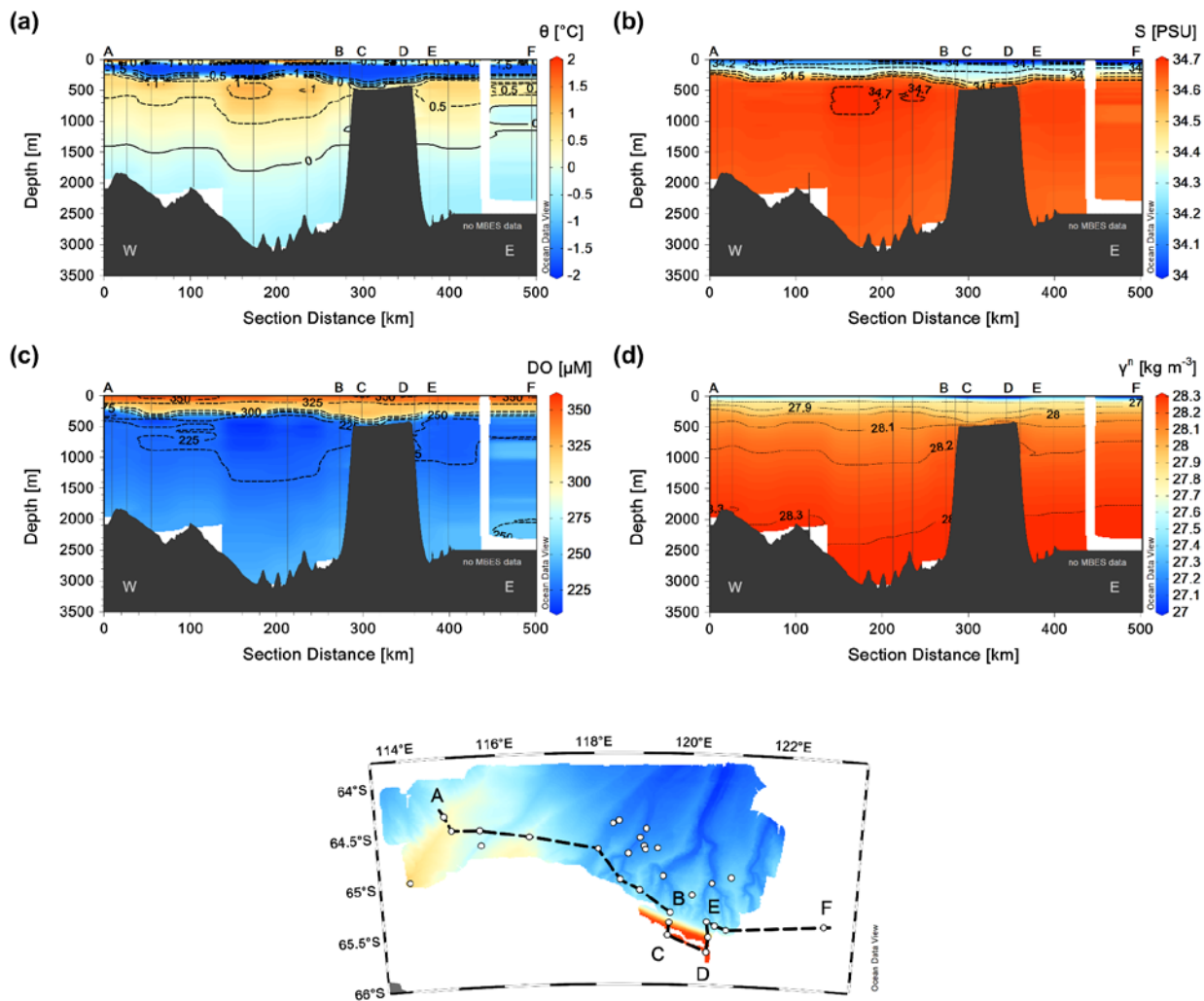


199

200 **Figure 3** - θ -S diagram (a) with colours referring to dissolved oxygen concentration (colorbar on the right). Characterization of
 201 the principal water masses, based on the continental shelf data according to Silvano et al. (2017, 2020): AASW - Antarctic surface
 202 water, WW - winter water, mCDW - modified Circumpolar Deep Water, AABW - Antarctic bottom water (with properties captured
 203 at 150°E), ISW - Ice Shelf Water and DSW - Dense Shelf Water. Zoom of the θ -S diagram (b) into the deepest layers where Bottom
 204 Depths (BD) are larger than 2000 m. Endmembers of RSBW - Ross Sea Bottom Water (red asterisk), ALBW - Adélie Land Bottom
 205 Water (blue), and CDW (green) are indicated (Thomas et al., 2020).

206 3.2 Spatial distribution of the hydrographic properties

207 To describe thermohaline properties in the study area and in proximity of the sea ice edge, we consider a zonal section (West-Est)
 208 running almost parallel to the continental slope, extending from station 6 to station 25 (Fig. 4), combined with two short cross-
 209 slope segments in correspondence of the shelf break. An overall distribution of θ , S, DO concentration, and neutral density indicates
 210 well defined layers of AASW, WW, and mCDW. AASW is situated in the relatively shallow surface layer (0 - 50 m depth), but
 211 with a wide range of temperature and salinity. Cold, fresh, and relatively uniform in temperature and salinity, WW lays beneath
 212 within the upper 400 m with larger thickness over the slope and shelf break. Beneath 400 m depth, warm and salty mCDW occupies
 213 the largest portion of the water column, decreasing its temperature and salinity approaching the shelf break (between positions C
 214 and D). There, it spreads over the continental shelf.

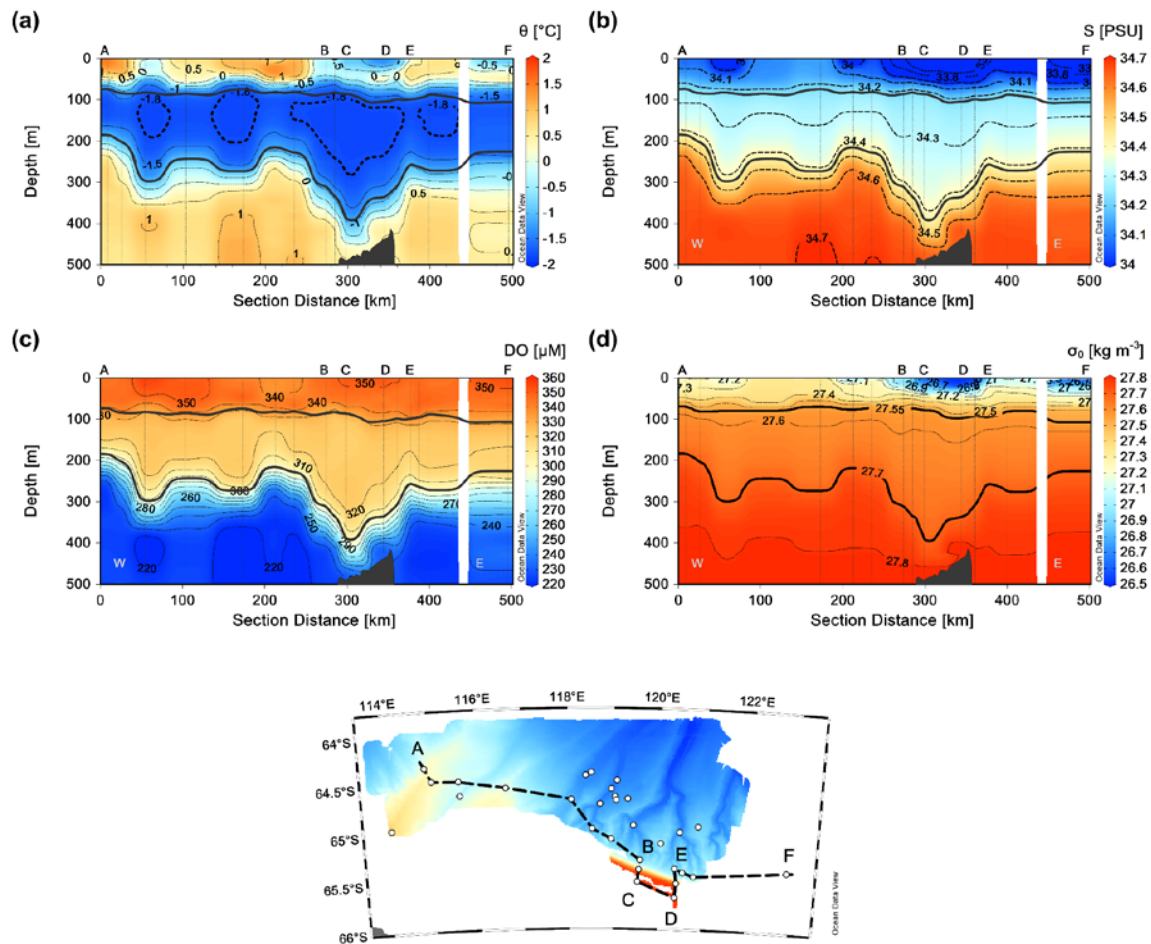


215

216 **Figure 4** - Along-slope transect (AB, CD, EF) against distance, with two across-slope segments BC and DE. Vertical sections of
 217 θ (a), S (b), DO concentration (c), and neutral density (d) over the entire depth range. See the insert map for the location of the
 218 transect.

219 A closer look into the upper 500 m layer reveals a well oxygenated AASW (Fig. 5). Its temperature and salinity decrease at the
 220 shelf break (area BCDE), probably due to the influence of cold and fresh ice melting water coming from the continental shelf (see
 221 Fig. 2b,c for the evolution of sea ice in January-February 2017). The portion of the water column occupied by WW, approximately
 222 between 50 m and 400 m depth, is cold ($-1.5^{\circ}\text{C} < \theta < -0.5^{\circ}\text{C}$), relatively fresh ($S < 34.45$), and well oxygenated ($\text{DO} > 300 \mu\text{M}$).
 223 The largest thickness of WW corresponds to the area approaching the continental shelf break (BCDE, water depths between 400

224 and 500 m), and it is typically associated with the downward tilting of density surfaces at the Fresh Shelf fronts, as described by
 225 Thompson et al. (2018).

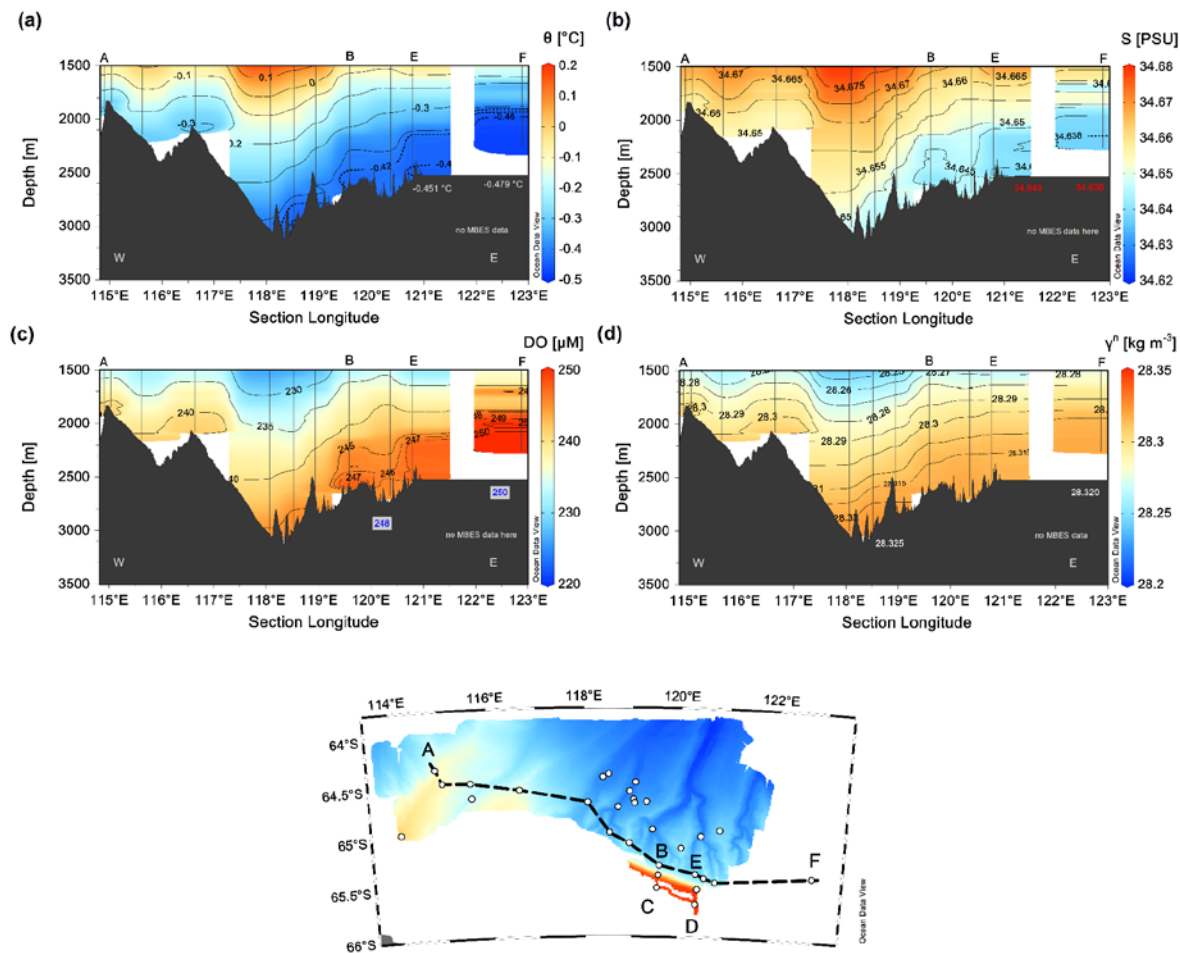


226

227 **Figure 5** - Along-slope transect (AB, CD, EF) against distance, with two across-slope segments BC and DE. Vertical sections of
 228 θ (a), S (b), DO concentration (c), and σ_0 referring to 0 dbar (d) in the upper 500 m. Thick black lines in each panel indicate
 229 isopycnals 27.55 and 27.70 kg m^{-3} , delimiting the layer occupied by WW (defined according to Silvano et al., 2017). See the insert
 230 map for the location of the transect.

231 From 500 m down to the continental slope and rise area, to depths greater than 3000 m, both temperature and salinity progressively
 232 decrease. Below 1500 m, in particular, cold waters have temperatures ranging from 0 $^{\circ}\text{C}$ to almost -0.5 $^{\circ}\text{C}$ near the bottom (Fig.
 233 6). The lowest temperature values (-0.479 $^{\circ}\text{C}$) are recorded in the easternmost part of the zonal transect, along with relatively low

234 salinity (38.638–38.640), and high oxygen (up to 248–250 μM) especially in the easternmost part of the section. The densest waters
 235 lay in the depressions/canyons/troughs between 118° and 119°E (neutral density 28.325 kg m^{-3}). Despite the relatively large
 236 distance among CTD stations, the sections of the thermohaline properties and dissolved oxygen concentration reveal that, close to
 237 the bottom, in correspondence of the canyons and rugged bottom morphology (i.e., near positions B and E in Fig. 6) there are
 238 signals of possible pathways of dense waters. The high resolution of the neutral density isolines makes it possible to detect how
 239 the isopycnals, and all other properties, follow the bottom morphology (Fig. 6).

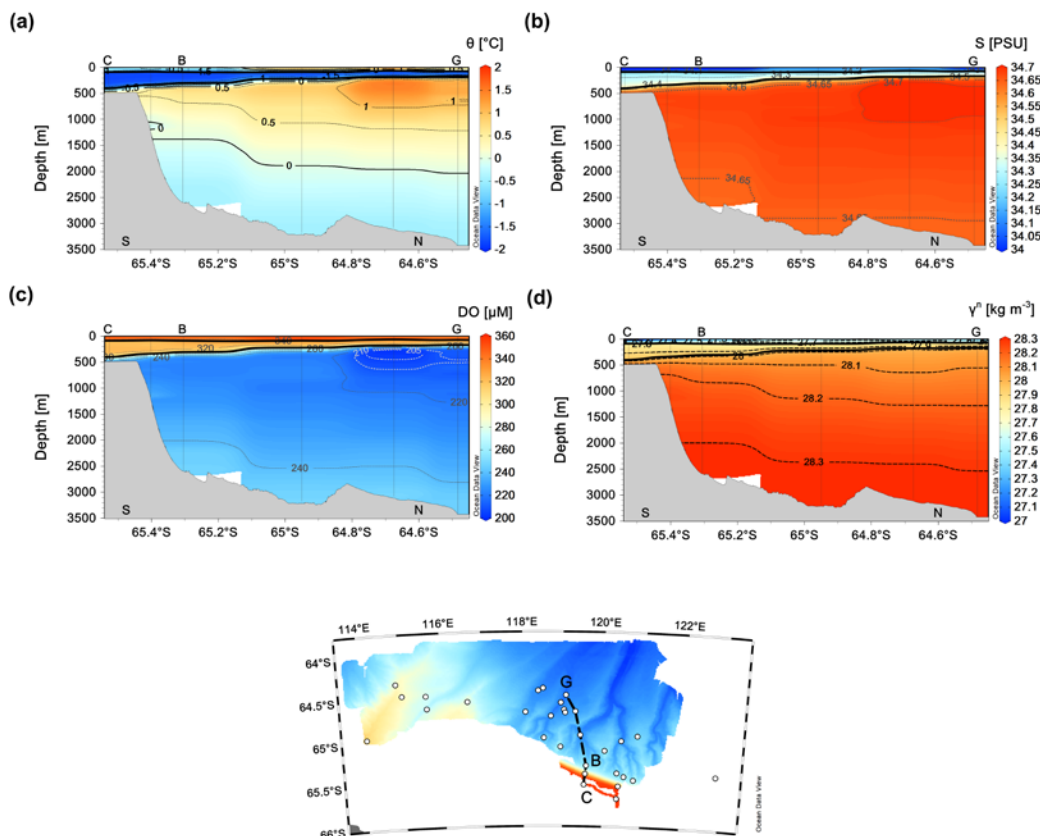


240

241

242 **Figure 6** - Along-slope transect ABEF against the geographical longitude. Vertical sections of θ (a), S (b), DO concentration (c),
 243 and neutral density (d) in the deep depth range (1500 m – bottom). The isoline steps are chosen to make evident small changes of
 244 the hydrographic properties near the bottom where waters are the coldest, the freshest, the densest, as well as rich in dissolved
 245 oxygen content. See the insert map for the location of the transect.

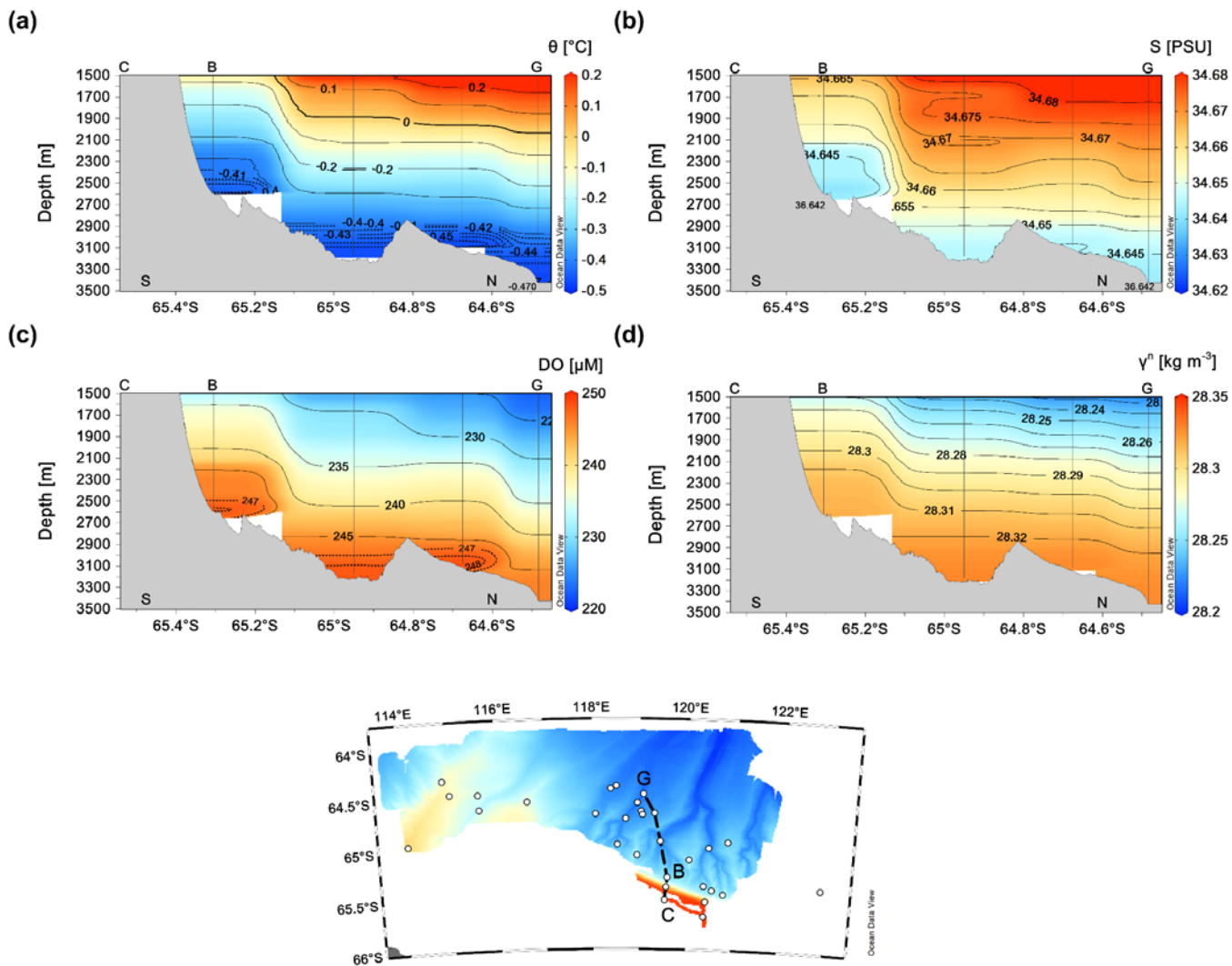
246 Patches of the deep and dense waters have properties that can be attributed to those of AABW (Figs. 3 and 4), which here seems
 247 influenced by ALBW rather than RSBW. CTD profiles at the deepest stations, which are within the canyons, are slightly saltier
 248 (see Fig. 3b) possibly due to the mixing either with the mCDW or with modified RSBW. From our data there is no clear evidence
 249 about the contribution of dense waters originating from the continental shelf. However, these processes could occur only in
 250 favourable conditions, e.g, during austral winters. The possible spread of such water out of the continental shelf area could give
 251 origin to density-driven flows that descend within canyons along the continental slope and could help shape the seafloor
 252 morphologies described by O'Brien et al (2020).



253

254 **Figure 7** - Across-slope transect CBG against the geographical latitude. Vertical sections of θ (a), S (b), DO concentration (c),
 255 and neutral density (d) over the entire depth range. Isopycnals of 27.55 and 27.7 kg m^{-3} are shown in all panels (thick black lines),
 256 delimiting WW (according to Silvano et al., 2017). See the insert map for the location of the transect.

257 To better identify the distribution of the water masses between the continental shelf and the off shelf area we draw a S-N across-
258 slope section. In fact, the transect CBG (see Fig. 7) illustrates a progressive thinning of the WW layer from the shelf break toward
259 the open sea, associated with the Antarctic Slope Front that separates cold and fresh shelf waters from the warm and salty mCDW
260 offshore (Thompson et al., 2018). Within the thick core layer of mCDW in the off shelf area, θ and S reach their maximum and
261 the DO content reaches its minimum between 64.6 °S and 64.8 °S. The layer occupied by mCDW progressively narrows in the
262 opposite direction toward the shelf break, where it also becomes less warm and less salty. There, the mCDW tongue protrudes
263 toward the shelf beneath the WW. On the continental slope, at approximately 1100 m depth, a slight temperature decrease appears
264 (Fig. 7a). However, the coarse space resolution between CTD stations precludes defining its origin. The deep and near-bottom
265 layers better illustrate how the isopycnals and associated thermohaline properties, along with the DO content, align with the
266 morphology of the sea floor (Fig. 8). There, coherent changes in θ , S, and DO point out at a cold, relatively fresh, and oxygenated
267 bottom layer, approximately 400-500 m thick, leaning on the continental slope and rise. Its well delimited characteristics fade
268 away from 64.6 °S northward.



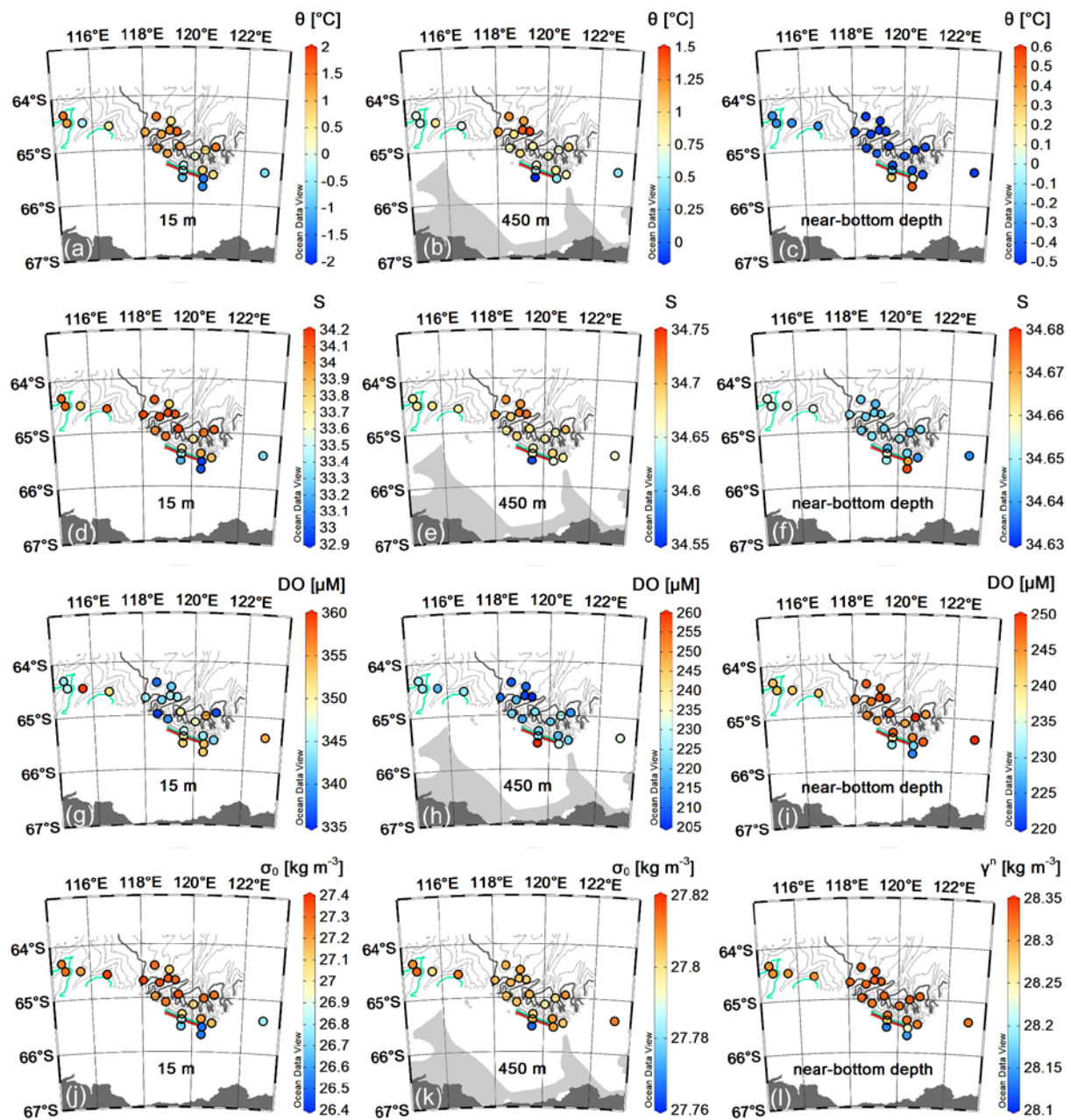
269

270 **Figure 8** - Same as figure 7 but with a zoom into the 1500 m - bottom layer. The isoline steps are chosen to make evident small
 271 changes of the hydrographic properties near the bottom where waters are the coldest, the freshest, the densest, as well as rich in
 272 dissolved oxygen content. See the insert map for the location of the transect.

273

274 The horizontal distribution of thermohaline properties near the surface (Fig. 9a, d, g, j) in the study area shows how they change
 275 in the across-slope direction, while they are more homogeneous along the direction parallel to the continental margin. From the
 276 shelf area, cold, fresh, and oxygenated waters approach the shelf break, where, due to their relatively low density, they mix with

277 other waters in the upper layer within the Antarctic Slope front. The strongest signal from shelf waters is visible at about 120°E
278 while fading in the northernmost portion offshore the study region, where higher values of θ and S (up to 2.0° C and 34.2,
279 respectively) are observed at 15 m depth. The 450 m depth horizon (Fig. 9b,e,h,k) is chosen to represent the core of the mCDW
280 (θ values > 0) in the offshore area, within a layer that extends from about 300 m down to 2000 m (Fig. 7). Here, S reaches its
281 maximum values, and DO its minimum. In the region between 118°E and 120° E, the mCDW probably finds its favorable pathway
282 to the continental shelf due to the bottom morphology. Approaching the shelf break, the mCDW mixes with other water masses
283 originating locally or transported by the Antarctic Slope Current westward along the continental margin. Close to the bottom (Fig.
284 9c,f,i,l), maxima θ and S with values of about 0.5°C and 34.678, respectively, are registered over the shelf break at the southernmost
285 station 25 (at ca. 120° E, 420 m depth). These large near-bottom values reflect the mCDW impinging on the slope beneath the
286 cold and fresh WW. Overall, in the westernmost part of the study area (115°E - 117°E) at depths around 2000 m, the bottom layer
287 is occupied by waters with θ around -0.30°C and S around 34.65-34.66, hence slightly warmer and saltier (and less dense) than
288 bottom waters found at similar depths in the central and eastern sectors (Fig. 9c,f). Yet, the fact that bottom waters in the western
289 sector, which is generally shallower than the eastern one (Fig. 6), have lower DO values suggests that this area is also influenced
290 by mCDW. Intrusions of mCDW onto the continental shelf, forced primarily by wind-driven upwelling (Greene et al., 2017;
291 Silvano et al., 2019), can occur where the shelf break is deeper than 400 m. Hence, mCDW can flow down the landward sloping
292 continental shelf, reaching the Totten Glacier grounding zone (Greenbaum et al., 2015; Nitsche et al., 2017; Silvano et al., 2017;
293 2019).



294
295 **Figure 9** - Near-surface (15 m depth), intermediate (450 m) and near-bottom θ (a, b, c), S (d, e, f), DO content (g, h, i), σ_θ (j, k) and
296 neutral density γ^n (l). The background bathymetry consists of isobaths (thin black curves) every 200 m obtained from MBES data
297 acquired during the 2017 campaign; thick lines indicate isobaths at 1000 m (red), 2000 m (cyan), and 3000 m (gray).

298

299

300 **4 Summary and conclusions**

301
302 Here we present oceanographic data (temperature, salinity, density, dissolved oxygen) collected offshore the continental margin
303 of the Sabrina coast (East Antarctica) between 113°E and 122°E and 66° S and 64°S, from the shelf edge to the continental rise
304 (Figs. 1 and 2). The water masses, described mainly according to their θ /S properties, are influenced by the seasonal heating and
305 freshening of the uppermost layers, and their spatial distribution appears to be linked to the complex morpho-bathymetric setting
306 of the study area. At about 400–500 m depth, the mCDW approaches shelf break in the area between 118 °E and 120 °E, around
307 64.5 °S, in good agreement with the numerical simulation results by Silvano et al. (2019). Small variations of the thermohaline
308 properties in the 400–500 m thick bottom layer in correspondence of the canyons revealed, instead, that there are signals of dense
309 waters with low θ and S values (-0.445 °C and 38.638 – 38.640, respectively) and relatively high DO values (240–250 μ M). Densest
310 waters, as shown in the θ -S plot (Fig. 3), have characteristics closer to typical ALBW than to RSBW. In general, mixing of these
311 dense waters with the mCDW is not excluded. Data also reveal that bottom layers at stations with depths greater than 3000 m (i.e.,
312 inside canyons) are occupied by water slightly saltier than that found at depths between 2000 and 3000 m, but with similar
313 temperatures. However, even though from our data there is no clear evidence about the contribution of dense waters originating
314 from the continental shelf, we cannot exclude that during winter and spring seasons, occasional dense water plumes may descend
315 and fill the deep layer, possibly mixing with the AABW. This hypothesis would support the fact that density-driven currents along
316 the steep slopes in the eastern portion of this region could contribute, on the one hand, to shaping the present-day, deeply-incised
317 canyons (Donda et al., 2020) and, on the other hand, to redistributing the different water masses (i.e., AASW, WW, and mCDW)
318 off the continental shelf beyond the shelf edge, favouring their mixing. Our data also reveal that in the western sector of the study
319 area (west of 118 °E) the bottom layer appears to be occupied by waters that are slightly warmer and saltier, as well as less
320 oxygenated, than those found in the central and easternmost sectors. This difference in the deep water properties of the two sectors
321 (eastern and western) seems to be an effect generated by the particular morphology of the seabed, being the western sector
322 shallower than the eastern one, and hence more easily influenced by mixing with the mCDW. In addition, ocean currents and
323 associated processes (along-slope flow, eddies, internal waves and tides, downslope density-driven currents) that involve local
324 water masses may be different in the two sectors. This implies that mCDW intrusions (Greene et al., 2017) and thus heat transport
325 on the Sabrina Coast continental shelf could be favoured by a combined effect induced by winds, eddies, and bathymetric
326 constraints (i.e., along slope canyons, Hirano et al., 2021).

327 The IN2017_V01 expedition was conducted during austral summer, when rapidly changing sea-ice conditions also influence the
328 near-surface and upper layers. The complex interplay of processes along the continental shelf, slope, and rise in this area is certainly
329 challenging, suggesting the importance of learning more about oceanographic dynamics during both winter and summer seasons.
330 In particular, the possibility of acquiring high temporal resolution data, especially during the winter period (e.g., by using long-
331 term in situ observatories), could help in the understanding of the oceanographic processes that have contributed to shape the distal
332 margin architecture and have influenced the evolution of the ice sheet.

333 **Data availability**

334 All data used in this work are archived in the enduring CSIRO Data Access Portal, <https://data.csiro.au> (direct link available at
335 https://www.marine.csiro.au/data/trawler/dataset.cfm?survey=IN2017_V01&data_type=ctd, last access on October 26, 2021).
336 Metadata records are made publicly available at <http://www.marlin.csiro.au>. Processed data and data products are, instead, publicly
337 available through Data Trawler <http://www.marine.csiro.au/data/trawler/index.cfm>, the MNF web data access tool
338 <http://www.marine.csiro.au/data/underway/>, and/or from national or world data centers most suitable for the dissemination of
339 particular data types (<https://doi.org/10.25919/yyex-t381>). All metadata entries should list this requested acknowledgment
340 statement where the data are presented or published (Armand et al., 2018).

341 **Declaration of Competing Interest**

342 The authors declare that they have no known competing financial interests or personal relationships that could have appeared to
343 influence the work reported in this paper.

344 **Acknowledgements**

345 We thank the Marine National Facility (<https://ror.org/01mae9353>), the IN2017_V01 scientific party, led by the Chief Scientists
346 L. Armand and P.E. O'Brien, MNF support staff and ASP crew members led by Capt. M. Watson for their help and support on
347 board the RV Investigator. We also thank Andres Roubicek and Dave Watts (CSIRO NCMI, Information and Data Centre) for the
348 assistance with data accessibility. This Project was supported through funding from the Australian Government's Australian
349 Antarctic Science Grant Program (AAS #4333) and the Australian Research Council's Discovery Projects funding scheme
350 (DP170100557). We would like also to acknowledge the financial support of the Italian National Antarctic Research Program
351 (Programma Nazionale di Ricerche in Antartide, PNRA) that funded the participation of the Italian team to the cruise through the
352 project TYTAN (Totten Glacier dYnamics and Southern Ocean circulation impact on deposiTional processes since the mid-IAte
353 CeNozoic) led by F. Donda.

354 **Author contribution**

355 M.B., V.K., and F.D. conceived and wrote the article. M.B. and V.K. processed the data used to prepare the figures and performed
356 the analyses. F.D. led the TYTAN project, L.K.A. and P.O. led the IN2017_V01 scientific cruise. L.A. contributed to collect
357 experimental data and participated in writing the text. All authors contributed to the discussion and revision of the manuscript.

358 **6 References**

359 Aytken A. R. A., Roberts, J. L., van Ommen T. D., Young D. A., Golledge N. R., Greenbaum J. S., Blankenship D. D. and Siegert
360 M.J.: Repeated large-scale retreat and advance of Totten Glacier indicated by inland bed erosion, doi:10.1038/nature17447, 2016.

361 Armand L. K, O'Brien P. E., and On-board Scientific Party: Interactions of the Totten Glacier with the Southern Ocean through
362 multiple glacial cycles (IN2017_V01), Post-survey report, Research School of Earth Sciences, Australian National University,
363 Canberra, <http://dx.doi.org/10.4225/13/5acea64c48693>, 2018.

364 Arroyo, M. C., Shadwick, E. H., and Tilbrook, B.: Summer Carbonate Chemistry in the Dalton Polynya, East Antarctica, 124,
365 5634–5653, <https://doi.org/10.1029/2018JC014882>, 2019

366 Bindoff, N. L., Rosenberg, M. A., and Warner, M. J.: On the circulation and water masses over the Antarctic continental slope and
367 rise between 80 and 150°E, Deep-Sea Res PT II, 47(12), 2299–2326, doi:10.1016/S0967-0645(00)00038-2, 2000.

368 Church, J.A., P.U. Clark, A. Cazenave, J.M. Gregory, S. Jevrejeva, A. Levermann, M.A. Merrifield, G.A. Milne, R.S. Nerem, P.D.
369 Nunn, A.J. Payne, W.T. Pfeffer, D. Stammer and A.S. Unnikrishnan, 2013: Sea Level Change. In: Climate Change 2013: The
370 Physical Science Basis. Contribution of Working Group I to the Fifth Assessment Report of the Intergovernmental Panel on
371 Climate Change [Stocker, T.F., D. Qin, G.-K. Plattner, M. Tignor, S.K. Allen, J. Boschung, A. Nauels, Y. Xia, V. Bex and P.M.
372 Midgley (eds.)]. Cambridge University Press, Cambridge, United Kingdom and New York, NY, USA.

373 De Conto, R. M. and Pollard, D.: Rapid Cenozoic glaciation of Antarctica induced by declining atmospheric CO₂. Nature, 421,
374 245–249, <https://doi.org/10.1038/nature012902003>, 2003.

375 Donda, F., Brancolini, G., O'Brien, P. E., De Santis, L., and Escutia, C.: Sedimentary processes in the Wilkes Land margin: a
376 record of Cenozoic East Antarctic Ice Sheet evolution. J Geol Soc London, 164, 243-256, <https://doi.org/10.1144/0016-76492004-159> 2007, 2007.

377 Donda, F., Leitchenkov, G., Brancolini, G., Romeo, R., De Santis, L., Escutia, C., O'Brien, P. E., Armand, L., Caburlotto, A., and
379 Cotterle, D: The influence of the Totten Glacier on the Late Cenozoic sedimentary record. Antarctic Science,
380 doi:10.1017/S0954102020000188, 2020.

381 Escutia, C., DeConto, R.M., Dunbar, R. De Santis, L., Shevenell, A. and Naish, T.: Keeping an eye on Antarctic Ice Sheet stability.
382 Oceanography 32(1):32–46, <https://doi.org/10.5670/oceanog.2019.117>, 2019.

383 Fretwell, P., Pritchard, H.D., Vaughan, D.G., Bamber, J.L., Barrand, N.E., Bell, R., Bianchi C., Bingham, R.G., Blankenship,
384 D.D., Casassa, G., and others. 2013. Bedmap2: Improved ice bed, surface and thickness datasets for Antarctica. Cryosphere 7:375–
385 393, <https://doi.org/10.5194/tc-7-375-2013>.

386 Greenbaum, J. S., Blankenship, D. D., Young, D. A., Richter, T. G., Roberts, J. L., Aitken, A. R. A., Legresy, B., Schroeder, D.
387 M., Warner, R. C., van Ommen, T. D., and Siegert, M. J.: Ocean access to a cavity beneath Totten Glacier in East Antarctica, Nat
388 Geosci, 8(4), 294–298, doi:10.1038/ngeo2388, 2015.

389 Greene, C. A., Blankenship, D. D., Gwyther, D. E., Silvano, A., and Wijk, E. van: Wind causes Totten Ice Shelf melt and

390 acceleration, 3, e1701681, <https://doi.org/10.1126/sciadv.1701681>, 2017.

391 Gulick, S., Shevenell, A., Montelli, A., Fernandez, R., Smith, C., Warny, S., Bohaty, S. M., Sjunneskog, C., Leventer, A.,
392 Frederick, B., and Blankenship, D. B: Initiation and long-term stability of the East Antarctic Ice Sheet in the Aurora Basin, *Nature*,
393 552, 225-241, doi: 10.1038/nature25026, 2020.

394 Gwyther, D. E., Galton-Fenzi, B. K., Hunter, J. R., and Roberts, J. L.: Simulated melt rates for the Totten and Dalton ice shelves,
395 *Ocean Science*, 10(3), 267–279, doi:<https://doi.org/10.5194/os-10-267-2014>, 2014.

396 Hirano, D., Mizobata, K., Sasaki, H., Murase, H., Tamura, T., and Aoki, S.: Poleward eddy-induced warm water transport across
397 a shelf break off Totten Ice Shelf, East Antarctica, *Commun Earth Environ*, 2, 1–8, <https://doi.org/10.1038/s43247-021-00217-4>,
398 2021.

399 Howat, I. M., Porter, C., Smith, B. E., Noh, M.-J., and Morin, P.: The Reference Elevation Model of Antarctica, *The Cryosphere*,
400 13, 665-674, <https://doi.org/10.5194/tc-13-665-2019>, 2019.

401 Huybrechts, P.: Glaciological modelling of the late Cenozoic East Antarctic Ice Sheet: stability or dynamism? *Geografiska Annaler*
402 Series A - Physical Geography

403 Khazendar, A., Schodlok, M. P., Fenty, I., Ligtenberg, S. R. M., Rignot, E., and van den Broeke, M. R.: Observed thinning of
404 Totten Glacier is linked to coastal polynya variability, *Nat Commun*, 4(1), 2857, doi:10.1038/ncomms3857, 2013.

405 Li, X., Rignot , E., Morlighem, M., Mouginot, J., and Scheuchl, B.: Grounding line retreat of Totten Glacier, East Antarctica, 1996
406 to 2013, *Geophys Res Lett*, 42(19), 8049-8056, doi:10.1002/2015GL065701, 2015.

407 Masson-Delmotte, V., Schulz, M., Abe-Ouchi, A., Beer, J., Ganopolski, A., González Rouco, J.F., Jansen, E., Lambeck, K.,
408 Luterbacher, J., Naish, T., Osborn, T., Otto-Bliesner, B., Quinn, T., Ramesh, R., Rojas, M., Shao, X., and Timmermann, A.:
409 Information from Paleoclimate Archives. In: *Climate Change 2013: The Physical Science Basis. Contribution of Working Group*
410 *I to the Fifth Assessment Report of the Intergovernmental Panel on Climate Change* [Stocker, T.F., D. Qin, G.-K. Plattner, M.
411 Tignor, S.K. Allen, J. Boschung, A. Nauels, Y. Xia, V. Bex and P.M. Midgley (eds.)]. Cambridge University Press, Cambridge,
412 United Kingdom and New York, NY, USA, 2013

413 Mohajerani, Y., Velicogna, I., and Rignot, E.: Mass Loss of Totten and Moscow University Glaciers, East Antarctica, Using
414 Regionally Optimized GRACE Mascons, *Geophys Res Lett* 45.14 7010-7018. doi: [10.1029/2018GL078173](https://doi.org/10.1029/2018GL078173), 2018.

415 Nitsche, F. O., Porter, D., Williams, G., Cougnon, E. A., Fraser, A. D., Correia, R., and Guerrero, R.: Bathymetric control of warm
416 ocean water access along the East Antarctic Margin, 44, 8936–8944, <https://doi.org/10.1002/2017GL074433>, 2017.

417 O'Brien, P. E. Post, A. L., Edwards, S., Martin, T. Caburlotto, Donda, F., Leitchenkov, G., Romeo, R., Duffy, M., Evangelinos,
418 D., Holder, L., Leventer, A., López-Quirós, A., Opdyke, B. N., and Armand, L. K: Continental slope and rise geomorphology
419 seaward of the Totten Glacier, East Antarctica (112°E-122°E), *Mar Geol*, 427, 106221,
420 <https://doi.org/10.1016/j.margeo.2020.106221>, 2020.

421 Pritchard, H. D., Arthern, R. J., Vaughan, D. G., and Edwards, L. A.: Extensive dynamic thinning on the margins of the Greenland

422 and Antarctic ice sheets, *Nature*, 461, 971–975, <https://doi.org/10.1038/nature08471>, 2009.

423 Pritchard, H. D., Ligtenberg, S. R. M., Fricker, H. A., Vaughan, D. G., van den Broeke, M. R., and Padman, L.: Antarctic ice-sheet
424 loss driven by basal melting of ice shelves, 484, 502–505, <https://doi.org/10.1038/nature10968>, 2012.

425 Rignot, E., Mouginot, J., and Scheuchl, B.: Antarctic grounding line mapping from differential satellite radar interferometry, 38,
426 <https://doi.org/10.1029/2011GL047109>, 2011.

427 Rignot, E., Jacobs, S., Mouginot, J., and Scheuchl, B.: Ice Shelf Melting Around Antarctica. *Science*, 341, 266–270.
428 doi:10.1126/science.1235798, 2013.

429 Rignot, E., Mouginot, J., Scheuchl, B., van den Broeke, M., and Morlighem, M.: Four decades of Antarctic Ice Sheet mass balance
430 from 1979–2017. *Proceedings of the National Academy of Sciences*, 116(4), 1095–1103. DOI: 10.1073/pnas.1812883116, 2019.

431 Rintoul, S. R., Silvano, A., Peña-Molino, B., van Wijk, E., Rosenberg, M., Greenbaum, J. S., and Blankenship, D. D.: Ocean heat
432 drives rapid basal melt of the Totten Ice Shelf. *Science Advances*, 2, 12, e1 601610, DOI:10.1126/sciadv.1601610, 2016.

433 Roberts, J. L., Warner, R. C., Young, D., Wright, A., Van Ommen, T. D., Blankenship, D. D., Siegert, M., Young, N. W., Tabacco,
434 I. E., Foieri, A., Passerini, A., Zirizzotti, A., and Frezzotti, M.: Refining broad-scale sub-glacial morphology of Aurora Subglacial
435 Basin, East Antarctica derived by an ice-dynamic-based interpolation scheme. *The Cryosphere Discussion*, 5, 655–684, 2011.

436 Schlitzer, R.: Ocean Data View, odv.awi.de, 2021.

437 Silvano, A., Rintoul, S. R., and Herraiz-Borreguero, L.: Ocean-Ice Shelf Interaction in East Antarctica, *Oceanography*, 29(4), 130–
438 143, 2016.

439 Silvano, A., Rintoul, S. R., Peña-Molino, B., and Williams, G. D.: Distribution of water masses and meltwater on the continental
440 shelf near the Totten and Moscow University ice shelves, *J Geophys Res-Oceans*, 122(3), 2050–2068, doi:10.1002/2016JC012115,
441 2017.

442 Silvano, A., Rintoul, S. R., Peña-Molino, B., Hobbs, W. R., Wijk, E. van, Aoki, S., Tamura, T., and Williams, G. D.: Freshening
443 by glacial meltwater enhances melting of ice shelves and reduces formation of Antarctic Bottom Water, *Sci. Adv.* 2018;4 :
444 eaap9467, <https://doi.org/10.1126/sciadv.aap9467>, 2018.

445 Silvano, A., Rintoul, S. R., Kusahara, K., Peña-Molino, B., van Wijk, E., Gwyther, D. E., and Williams, G. D.: Seasonality of
446 Warm Water Intrusions Onto the Continental Shelf Near the Totten Glacier, 124, 4272–4289,
447 <https://doi.org/10.1029/2018JC014634>, 2019.

448 Silvano, A., Foppert, A., Rintoul, S. R., Holland, P. R., Tamura, T., Kimura, N., Castagno, P., Falco, P., Budillon, G., Haumann,
449 F. A., Naveira Garabato, A. C., and Macdonald, A.: Recent recovery of Antarctic Bottom Water formation in the Ross Sea driven
450 by climate anomalies, *Nature Geoscience*, 13, 780–786, doi: 10.1038/s41561-020-00655-3, 2020.

451 Smith, J. A., Hillenbrand, C.-D., Kuhn, G., Larter, R. D., Graham, A. G. C., Ehrmann, W., Moreton, S. G., and Forwick, M.:
452 Deglacial history of the West Antarctic Ice Sheet in the western Amundsen Sea Embayment, *Quaternary Science Reviews*, 30,

453 488–505, <https://doi.org/10.1016/j.quascirev.2010.11.020>, 2011.

454 Tamura, T., Ohshima, K. I. and Nihashi, S.: Mapping of sea ice production for Antarctic coastal polynyas, *Geophys. Res. Lett.*,
455 35, L07606, doi:10.1029/2007GL032903, 2008.

456 Thomas, G., Purkey, S. G., Roemmich, D., Foppert, A., Rintoul, S. R.: Spatial variability of Antarctic bottom water in the
457 Australian Antarctic Basin from 2018–2020 captured by Deep Argo. *Geophysical Research Letters*, 47, e2020GL089467.
458 <https://doi.org/10.1029/2020GL089467>, 2020.

459 Thompson, A. F., Stewart, A. L., Spence, P., and Heywood, K. J.: The Antarctic Slope Current in a Changing Climate, 56, 741–
460 770, <https://doi.org/10.1029/2018RG000624>, 2018.

461 Wakatsuchi, M., Ohshima, K. I., Hishida, M. and Naganobu, M.: Observations of a street of cyclonic eddies in the Indian Ocean
462 sector of the Antarctic Divergence. *Journal of Geophysical Research*, 99(C10), 20,417–20,426,
463 <https://doi.org/10.1029/94JC01478>, 1994.

464 Williams, G. D., Meijers, A. J. S., Poole, A., Mathiot, P., Tamura, T., and Klocker, A.: Late winter oceanography off the Sabrina
465 and BANZARE coast (117–128°E), East Antarctica, *Deep Sea Research Part II: Topical Studies in Oceanography*, 58, 1194–1210,
466 <https://doi.org/10.1016/j.dsrr.2010.10.035>, 2011.

467 Wright A. P., Young, D. A., Roberts, J. L., Schroeder, D. M., Bamber, J. L., Dowdeswell, J. A., Young, N. W., Le Brocq, A. M.,
468 Warner, R. C., Payne, A. J., Blankenship, D. D., van Ommen, T. D., and Siegert, M. J.: Evidence of a hydrological connection
469 between the ice divide and ice sheet margin in the Aurora Subglacial Basin, East Antarctica. *J Geophys Res*, 117, F01033,
470 doi:10.1029/2011JF002066, 2012.

471 Young, D. A., Wright, A. P., Roberts, J. L., Warner, R. C., Young, N. W., Greenbaum, J. S., Schroeder, D. M., Holt, J. W., Sugden,
472 D. E., Blankenship, D. D., Van Ommen, T. D., and Seigert, M. J.: A dynamic early East Antarctic Ice Sheet suggested by ice
473 covered fjord landscapes, *Nature*, 474, 72–75, <https://doi.org/10.1038/nature10114>, 2011.